Inhibition effect of lithium salts on the corrosion of AA1100 aluminium alloy in ordinary Portland cement pastes

Xiang Li [a,b], Sébastien Caes [a], Thomas Pardoen [b], Geert De Schutter [c], Tom Hauffman [d], Bruno Kursten [a]

[a] SCK·CEN, Boeretang 200, B-2400 Mol, Belgium

[b] Institute of Mechanics, Materials and Civil Engineering (IMMC), Université catholique de Louvain, B-1348 Louvain-la-Neuve, Belgium

[c] Magnel-Vandepitte Laboratory, Department of Structural Engineering and Building Materials, Technologiepark-Zwijnaarde 60, B-9052 Ghent (Zwijnaarde), Ghent University, Belgium

[d] Department of Materials and Chemistry, Research Group Electrochemical and Surface Engineering (SURF), Vrije Universiteit Brussel, Pleinlaan 2, 1050 Brussels, Belgium

Abstract

The corrosion inhibition effect of lithium nitrate and lithium carbonate has been investigated for protecting aluminium alloy 1100 encapsulated in ordinary Portland cement pastes. A combined approach of electrochemical measurements, scanning electron microscopy and gas chromatography revealed that the corrosion rate of AA1100 is effectively inhibited owing to the formation of a protective corrosion product film in cement pastes with the addition of $LiNO_3$ or Li_2CO_3. Without any inhibitor, the fast corrosion rate leads to visible cracking in the cement paste matrix. Both the hydration evolution and the curing environment of cement pastes play important roles in the corrosion process.

Keywords

Aluminium; Lithium salts; Corrosion inhibition; Ordinary Portland cement; Electrochemical impedance spectroscopy; Scanning electron microscopy; Gas chromatography

1. Introduction

Aluminium alloy 1100 (AA1100) has been chosen as the nuclear fuel cladding in Belgian Reactor 1 (BR1) owing to a high thermal conductivity, a low thermal neutron absorption cross section, a high oxidation resistance and excellent mechanical properties [1,2]. Once BR1 fuel will eventually

become radioactive nuclear waste, one possible option for the long-term management of BR1 fuel is the geological disposal. In this disposal, the innermost barrier used to immobilise radioactive materials, is the direct encapsulation of the spent fuel in a cement paste matrix [3]. Hence, the aluminium cladding, as the outer most material of BR1 fuel, will be in contact with the cement paste matrix.

Ordinary Portland Cement (OPC) is one of the most widely applied materials for the encapsulation of radioactive wastes. However, the highly alkaline pore solution in OPC pastes (pH normally above 12.5 [4]), can lead to a high corrosion rate of aluminium alloy 1100 (AA1100) in the geological disposal, because the passive aluminium oxide layer cannot be steadily maintained on the surface of Al when pH is above 8.6 [5]. Without the protection of this dense aluminium oxide layer, the continuous corrosion process increases the breach risk of the aluminium cladding, and can potentially lead to the leakage of inner radioactive materials. Moreover, the production of H_2 gas and the fast accumulation of corrosion products, which results in volume changes compared to the metallic aluminium, raises the internal stress and consequently induces cracks in the cement paste matrix. Such a cracking phenomenon was reported by L.M. Spasova et al. [6] and Q. Zhou et al. [7] for the corrosion of Al embedded BFS/OPC system. Therefore, this study is dedicated to finding a solution for inhibiting the corrosion of AA1100 in ordinary Portland cement pastes.

For closed systems, such as the one stored in the geological disposal of nuclear waste, it is convenient to make use of corrosion inhibitors owing to a relatively stable concentration over a long timescale with a low possibility of dilution. Meanwhile, in a geological repository environment (radioactivity, high temperature, high pH…) of nuclear waste, organic compounds can be deteriorated and the use of inorganic salts is therefore theoretically favoured. Many investigations focused over the last decades on studying different lithium salts, such as $LiNO_3$ and Li_2CO_3, as potential inhibitors for the corrosion of Al alloys in alkaline systems [8-11]. For aluminium encapsulated in cementitious materials, researchers reported that mixing $LiNO_3$ with cement resulted in the inhibition of hydrogen gas generation produced during the corrosion of Al in cement pastes and mortars [12-14]. This inhibition effect of lithium salts on the corrosion of aluminium in high pH conditions is attributed to the formation of a Li-Al layered double hydroxide

(LDH) preservation film on the aluminium surface. This LDH film results from the facile intercalation of lithium ions into the aluminium hydroxide layer to form a layered double hydroxide ($[LiAl_2(OH)_6]_n^{1+} \cdot X^{n-} \cdot yH_2O$, where X^{n-} is the counter ion of the lithium salt added in the cement paste (NO_3^- or CO_3^{2-} when $LiNO_3$ or Li_2CO_3 is added, respectively)) [10,15]. LDH-based films were reported to possess high corrosion resistance constituting thus a physical barrier against water and ions migration [16]. Toshiaki et al. proved the insolubility of the Li-Al LDH film both theoretically and experimentally [13,17] and investigated the influence of underground water on the stability of the Li-Al LDH film in geological disposal conditions [18,19]. The hydrogen production during the corrosion of Al in cement pastes was also found to be inversely proportional to the amount of added $LiNO_3$, but a dosage higher than 3 % of the cement weight does not further improve the inhibition ability [13]. Li_2CO_3, as a potential substitute of $LiNO_3$, also shows inhibition ability regarding Al corrosion in high pH systems [20-24]. While being added into cement pastes, the CO_3^{2-} ions are also likely to affect the corrosion process by changing the microstructure of cement pastes through a carbonation reaction. Besides, Li_2CO_3 has a mitigation function for the alkali silica reaction (ASR) in OPC mortar and concrete systems and hence effectively reduces the possibility of cracking caused by ASR [25-27].

The objective of this study was to investigate the corrosion inhibition effect of $LiNO_3$ and Li_2CO_3 on AA1100 embedded in OPC pastes by a combination of different methods. First, the corrosion mechanisms and the corrosion rates were investigated by electrochemical techniques i.e. Electrochemical Impedance Spectroscopy (EIS) and Tafel polarization tests. Then, the morphology and the chemical composition of the aluminium/corrosion product film/cement paste interface was studied by Scanning Electron Microscopy (SEM) and Energy-Dispersive X-ray spectroscopy (EDX). The evolution of the corrosion product film thickness was also determined by SEM in order to calculate the corrosion rate. Furthermore, the hydrogen gas produced during the corrosion reaction was also measured by Gas Chromatography (GC) to estimate the corrosion rate. Finally, two different curing conditions were adopted to understand the influences of the curing conditions of the cement pastes on the corrosion process.

2. Experimental procedures

2.1. Sample preparation

The aluminium alloy 1100 used in the experiments was obtained from Alfa Aesar, with a nominal chemical composition consisting of a minimum of 99.0% Al and 1.0% Si + Fe. Test specimens were cut from a 1.0 mm thick sheet with two different dimensions depending on the type of experiment: larger Al plates (30x30 mm) were used for the electrochemical measurements, while smaller Al plates with 2.25 cm^2 surface area (15x15 mm) were used for GC and SEM measurements. These sheets were ground with successive grades of SiC paper up to 1200 grid, and then cleaned with acetone, ethanol, and distilled water, respectively before to be dried by air flow.

Ordinary Portland Cement (CEM I 52.5 N class according to EN 197-1) was used to produce the cement pastes. Its chemical composition is provided in Table 1.

Table 1. Chemical composition of the cement.

Composition	SO_3	Cl	Na_2Eq	SiO_2	Al_2O_3	Fe_2O_3	CaO	Na_2O	K_2O	MgO	Others
wt%	2.60	0.04	0.66	21.3	5.2	3.3	63.1	0.33	0.50	2.19	0.78

Three different OPC pastes were prepared in this study: pure OPC, OPC+$LiNO_3$ and OPC+Li_2CO_3. The pure OPC paste was used as a reference and possessed a low water-to-cement ratio (w/c) equal to 0.36. For the production of the OPC+$LiNO_3$ pastes, 3 wt.% of $LiNO_3$ was added to the cement because this concentration can effectively inhibit the generation of hydrogen and a higher dosage cannot further improve the inhibiting effect [13]. The w/c was equal to 0.36. For the production of OPC+Li_2CO_3, 1.607 wt.% of Li_2CO_3 was added to the system to keep the same lithium ions concentration. The addition of Li_2CO_3 increased the viscosity of the cement paste. Therefore, the w/c was increased up to 0.5 to improve the workability of this cement paste.

For all systems, the mixture of cement powder and milli-Q water was stirred manually for 10 minutes in a glove box under argon atmosphere in order to limit as much as possible the quantity of oxygen in the system (less than 1 ppm O_2) to mimic the deep geological conditions.

The electrochemical experiments (EIS & Tafel) were performed using a two-electrode configuration, whose feasibility for electrochemical tests was already examined elsewhere [28-30]. The working electrode and the counter/reference electrode were identical. To allow an easy connection of the electrodes embedded in the cement paste, an aluminium wire was spot-welded at the back of the 30x30x1 mm Al plates. The electrodes were covered by a non-conductive and waterproof tape and the Al wire were surrounded by a Teflon® heat shrinkable tube, leaving an exposed surface area of 2.26 cm². Finally, the Al plates were positioned in parallel at a distance of 5.5 mm apart by means of Teflon® screws and plastic rods. Once the fresh cement paste was poured into a 40×40×40 mm cubic mould, the two-electrode system was immediately inserted into the middle of the cement paste as shown in Figure 1(a) and covered by a plastic sheet on the surface to avoid too fast water evaporation.

Samples prepared for the GC and SEM analyses used the same cubic mould. The fresh cement paste was firstly poured into the mould and then a 15x15x1 mm Al plate was inserted into the centre of the mould (Figure 1(b)).

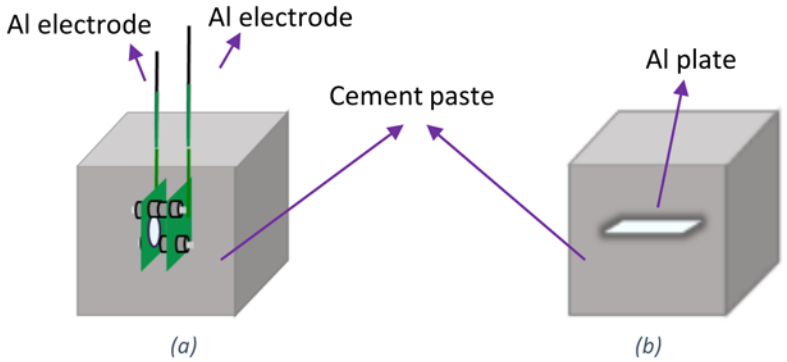

Figure 1. Schematics of EIS & Tafel (a) and SEM & GC (b) specimens.

All specimens were de-moulded after 24 h and were cured in two types of conditions (Part 1 in the supplementary material). In condition 1, the specimens, containing the Al plates, were placed in a humid Ar atmosphere. The humid atmosphere is produced by inserting the specimens on a holder above the water level in a closed cell. This environment also simulates the humid and anaerobic underground environment in the real geological disposal. After about 80 days, when the corrosion rates reach a steady state for OPC+$LiNO_3$ and OPC+Li_2CO_3 samples (see Figure 8(a) and Figure 9(a)), these samples were transferred into a saturated $Ca(OH)_2$ solution i.e. limewater to simulate the resaturation of the cement paste after possible breaching of the waste protective

barrier. In condition 2, the specimens were directly immersed and cured in saturated $Ca(OH)_2$ solution from the beginning. For electrochemical and GC tests, three repetitive samples were prepared for each condition to ensure the replicability of the results. For SEM characterization, one sample was made for each selected time point to reveal the corrosion variation as a function of time.

2.2. Methods

The corrosion rate was estimated for all samples using three different techniques: (i) EIS via the calculation of the transfer resistance after fitting the curves, (ii) GC via the production of hydrogen and (iii) SEM via the direct measurement of the corrosion product layer with time.

2.2.1. EIS & Tafel

The electrochemical measurements were performed using an Autolab PGSTAT 30 potentiostat combined with the NOVA 1.8 version software. EIS spectra were recorded at the open circuit potential with a 10 mV amplitude. The frequency ranged between 10^6 Hz to 10^{-2} Hz, with 10 frequency values per logarithmic decade. The analysis and the fit of the spectra were performed using the software 'Zview'. Tafel plots were measured potentiodynamically from -0.25 V to +0.25 V vs. OCP with a scanning rate of 0.167 mv/s. The Tafel results were then used to determine the cathodic slope β_c and anodic slope β_a by extrapolation of the corrosion current curves.

The fitting of EIS spectra (more details are provided in Section 3.2) provides the values of the charge transfer resistance (R_t) in the corrosion process. Using this value, the corrosion current, I_{corr}, is calculated by the Stern-Geary equation (Eq. (1)) [31,32]:

$$I_{corr} = \frac{1}{2.3R_t}\left(\frac{\beta_a\beta_c}{\beta_a + \beta_c}\right), \quad (1)$$

where β_a and β_c are the slopes of the Tafel curves and were determined from Tafel measurements.

The corrosion rate (ν_{corr}) is then calculated using Eq. (*2*) :

$$v_{corr}\ (in\ m \cdot y^{-1}) = 3.27 \times \frac{I_{corr}}{\rho} \times EW\ , \qquad (2)$$

where ρ is the metal density (g·cm^{-3}, ρ_{Al} = 2.7 g·cm^{-3}) and *EW* is equivalent weight. *EW* is calculated by dividing the atomic weight of an element with the valence of the metal, hence, for Al atomic weight is 27 and the valence is 3, so EW_{Al} = 27/3 = 9.

2.2.2. GC

GC technique was used to monitor the volume of hydrogen produced with time. The specimens were stored in a gas-tight container and the hydrogen gas concentration inside the container was measured by a Shimadzu GC-2010 Plus type GC equipment on a regular basis. Because the container volume is known, the amount of hydrogen generation over a given time interval can be determined and correlated to the corrosion rate of Al plates in cement pastes. The atmosphere in the container was thoroughly refreshed by Ar every time after the measurement to remove the residual hydrogen generated during the previous period.

GC provides the amount of hydrogen generated during a specific period. In high pH systems, the amount of the consumed aluminium is linked to that of the formed hydrogen by the following reaction:

$$Al + 3H_2O + OH^- \rightarrow Al(OH)_4^- + \frac{3}{2}H_2 \uparrow . \qquad (3)$$

Therefore, the consumed Al can be quantitatively determined and the average corrosion rate over a certain period can be calculated as follow:

$$v_{corr} = \frac{Al\ corroded}{time}\ (\mu m \cdot y^{-1})\ . \qquad (4)$$

2.2.3. SEM & EDX

The corrosion product film thickness was also analysed as a function of time by SEM. One specimen was cut and prepared at each selected time point. SEM-EDX characterization was carried out with a Phenom Pro X apparatus using an accelerating voltage of 15 kV and a working distance fixed automatically. As there is no internal standard in the apparatus, EDX only provides semi-quantitative analysis. The thickness variation of the corrosion product film extracted from SEM micrographs is then used to calculate the corrosion rate. The mean thickness at each time point is determined from 12 thickness measurements performed at different locations of a SEM sample. Then, the average corrosion rate during a time interval can be calculated using:

$$v_{corr}\ (in\ \mu m \cdot y^{-1}) = \frac{T_{t_2} - T_{t_1}}{t_2 - t_1}, \quad (5)$$

where T_{t_1}, T_{t_2} are the mean thickness values of the corrosion product film at times t_1 and t_2.

The SEM method is not suitable for pure OPC samples, because severe cracks emerges in the cement paste just after a few days, which interferes the normal growth of corrosion product film. Meanwhile, it is difficult to identify the boundary between the corrosion product film and the cement paste in some pure OPC samples, which brings some uncertainty in the determination of the film thickness. More details, e.g. the cracks in the cement paste and the delamination of the corrosion product film, from SEM analysis are provided in Section 3.5, while the study of v_{corr} using the SEM method is provided together with EIS and GC in Section 3.3.

3. Results and discussion

3.1. Impedance spectrum

The impedance spectra of pure OPC samples (Figure 2) show that three time constants can be visiblely recognized. The Nyquist plot exhibits the first semicircle describling the charge transfer process in the high-frequency domain with the aluminium/corrosion product film/cement paste interfacial response at the low-frequency limit. An additional intermediate semicircle is recognized in the Hz region, which corresponds to the cement paste [33,34].

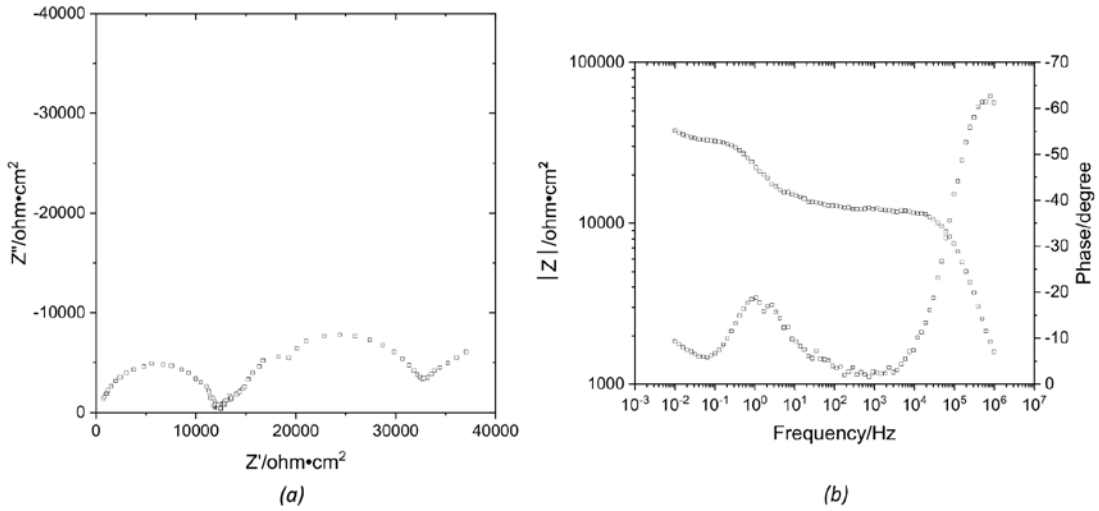

Figure 2. Nyquist (a) and Bode (b) plots of AA1100 aluminium alloy in the OPC paste after 13 days in condition 1.

For samples with the addition of $LiNO_3$ or Li_2CO_3, the three time constants are also found in the high-frequency domain, around the Hz domain and in the low-frequency domain, respectively. Exceptionally, for one OPC+Li_2CO_3 sample, the fourth time constant in the range of 1KHz ~ 10KHz is occasionaly observed at the early stage of the tests. This time constant is gradually overlapped by the other time constants with the increase of time (see Figure 3(b)). The impedance spectrum plots evolve as a function of time, increasing the difficulty of distinguishing each time constant as shown in Figure 3(a). At the early stage of the tests, with the ongoing of the cement hydration process, the thickening of the corrosion product film and the increase of the charge transfer resistance, the magnitude of the impedance at the low-frequency limit increases monotonically (see Figure 3(a)). Afterwards, other factors e.g. the ingress of cement pore solution into the

corrosion product film, can lead to a drop of the impedance magnitude at the low-frequency limit as shown in Figure 3(c).

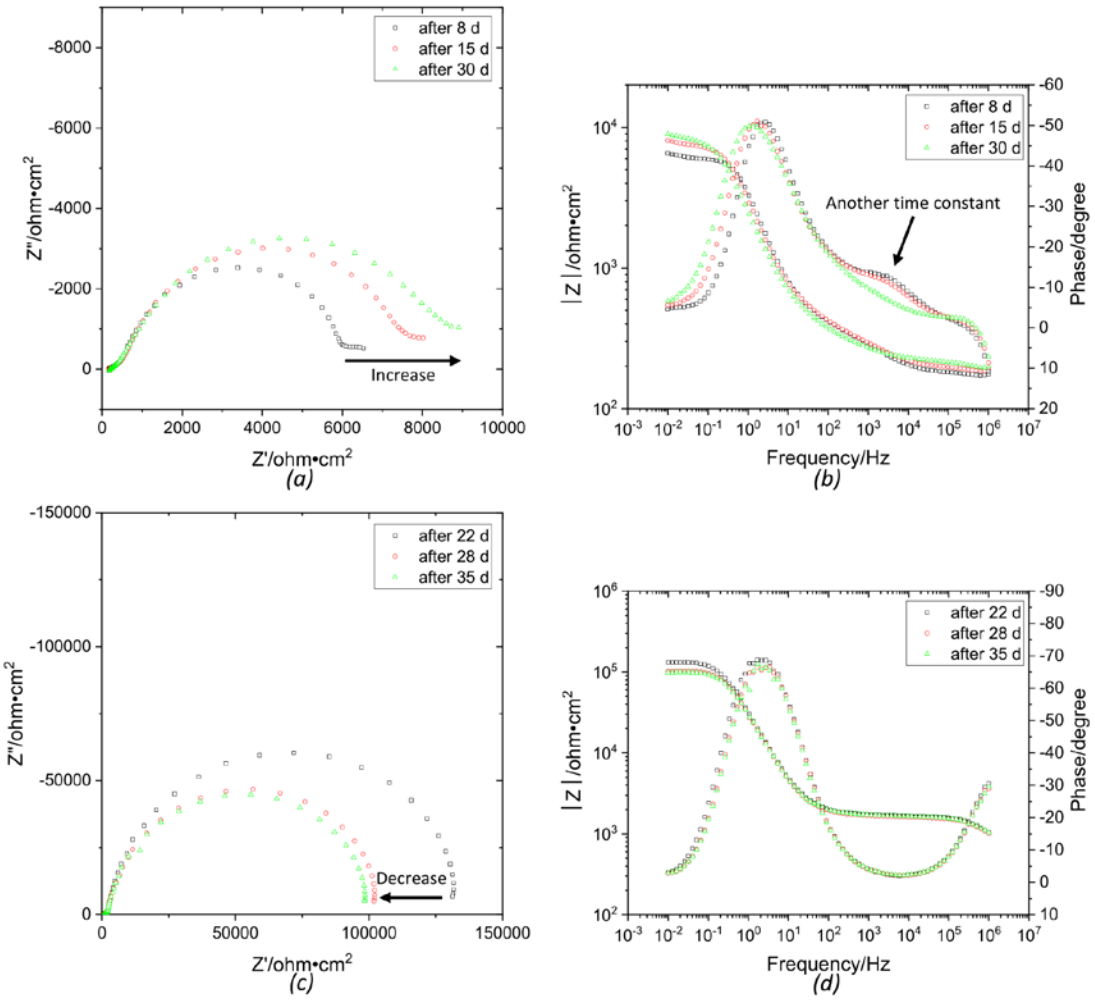

Figure 3.The variation of Nyquist (a) and Bode (b) plots of AA1100 in the OPC+Li_2CO_3 paste in condition 2 and the variation of Nyquist (c) and Bode (d) plots of AA1100 in the OPC+$LiNO_3$ paste in condition 1.

3.2. Equivalent circuit model

To quantitatively analyse the electrochemical spectrum results, the EIS fitting (part of the fitting results are provided in Section 7 in the supplementary material) was performed using the electrical equivalent circuit (EEC) shown in Figure 4, which was established based on the physical structures of the cell. This circuit can be divided into three different parts.

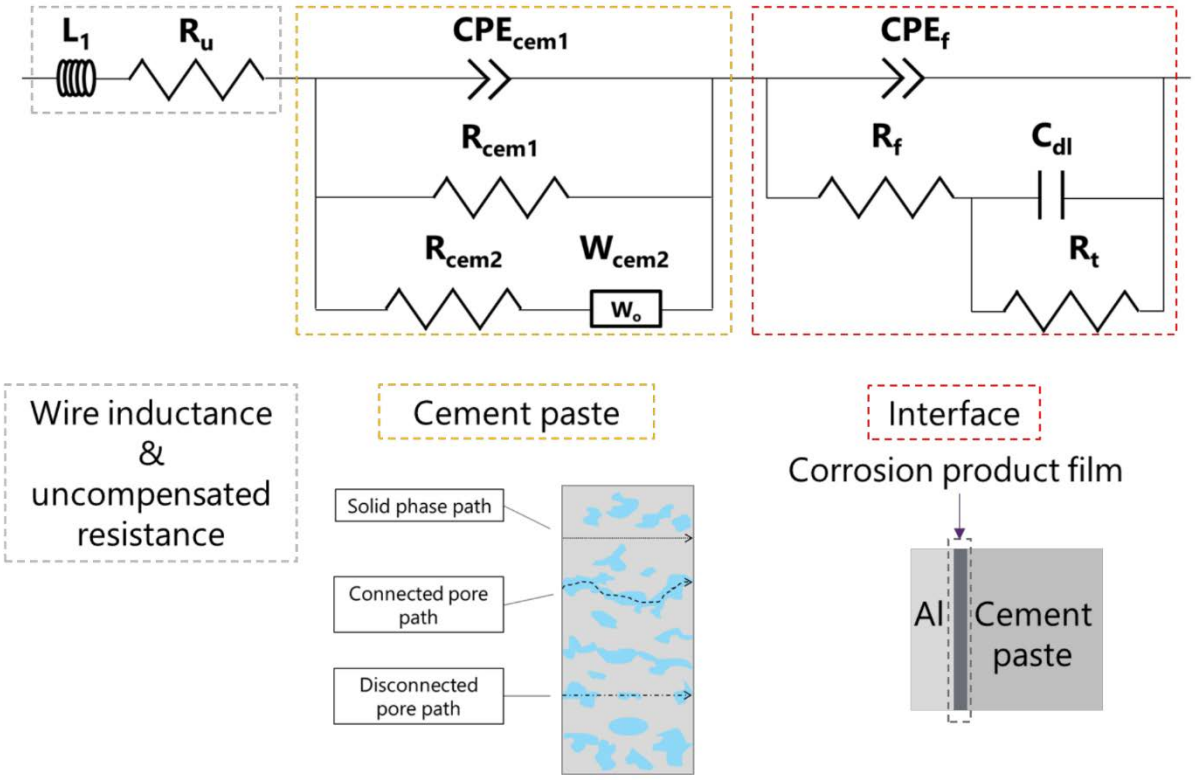

Figure 4. Electrical equivalent circuit employed to fit EIS spectra for the corrosion of Al plate in cement pastes.

First, an inductor (L_1) and a resistor (R_u) are placed in series. L_1 represents the inductance of external wires. This term was used when the high frequency (1 MHz), adopted to collect the information of the cement paste, activates the inductance response in some samples. R_u, an overall uncompensated resistance, includes the resistance of the solution that exists in macro holes or crevices, the resistances of the Al plate matrix, Al rods, the external circuit, etc. L_1 and R_u can be selected or not according to the appearance of a specific impedance spectrum and such an adjustment has little influence on the other subcircuits.

The second part of the EEC is composed of three branches in parallel corresponding to the electrochemical properties of the cement paste between two electrodes. CPE_{cem1} represents the

capacitance properties of the solid phase in the cement paste; R_{cem1} is the resistance of ionic conduction through the connected capillary pores; the disconnected pore path is composed of a resistor (R_{cem2}) and a Warburg element (W_{cem2}), which correspond to the charge transfer processes of the pore phase and solid phase, respectively. A similar EEC model, which describes the cement paste, is reported in the literature [34-36]. The only difference is that a constant phase element (CPE_{cem2}) was used in the literature instead of a Warburg element (W_{cem2}). Based on the fitting results in this study (see Section 2 in the supplementary material), the charge transfer in the solid phase between disconnected pores is more likely to be controlled by ion diffusion process (the ion diffusion in cementitious materials was also mentioned by literature [37-40]). Hence, the Warburg element was chosen as it fits more correctly the physical system observed in this study.

The third part accounts for the electrochemical response of the aluminium/corrosion product film/cement paste interfaces on the two electrodes. The same EEC was adopted by Visser et al. [23] for the corrosion study of aluminium alloy 2024 in alkaline lithium carbonate solution. CPE_f (C_f is occasionally used when the '*n*' value of CPE_f is above 1) and R_f represent the capacitance and the resistance properties of the corrosion product film, respectively. C_{dl} is the double layer capacitance. R_t is the charge transfer resistance, which describes the charge transfer process. Considering the setup composed of two identical electrodes, the magnitude of the resistances (R_f and R_t) in this part is actually the sum of two individual elements coming from both electrodes. Thus, the real R_f and R_t in each electrode are half of the fitted value. For the same reason, the real *Q* parameters of CPE_f and C_{dl} are twice as high as the fitted value.

Ignoring the contribution of the first part (L_1 and R_u), which only emerges occasionally, the EEC model used in this study normally involves four time constants related to CPE_{cem1}, W_{cem2}, CPE_f and C_{dl}. However, in general, most of the spectra only show 3 time constants visually (an example is shown in Figure 2), which matches the results reported in literature [14]. This apparent contradiction is attributed to the convolution of electrochemical phenomena happening at closeby frequencies with an amplitude in the same order of magntitude.

3.3. Corrosion rates

A comparison of the corrosion rates, measured with EIS and GC, of pure OPC samples tested in condition 1 is illustrated in Figure 5(a). The corrosion rates from both techniques show a decreasing trend from around 200 $\mu m \cdot y^{-1}$ to 30 $\mu m \cdot y^{-1}$ at the beginning of the cement hydration. This obvious decrease can be linked to the hydration of the cement paste and the accumulation of the corrosion products. The water content in the cement paste declines as a function of the hydration degree and hence induces a decrease of the corrosion rate. Besides, the accumulation of corrosion products forms a thicker physical barrier, which is also able to inhibit the corrosion rate. The main difference between EIS and GC is that the corrosion rate from GC is behind that from EIS in terms of time as if the corrosion rate from GC is the translational displacement of that from EIS. This can be explained by the different characteristics of the two methods. The corrosion rate from GC is actually the average corrosion rate over the period before the time point, while the rate from EIS is the real-time value. Therefore, a delay shift can occur in GC results. Besides, the different configurations are likely to cause discrepancies because of the differences in the exposed areas and positions in the bulk of the cement paste that can affect the diffusion process of reactants and products. After 40 days, the EIS tests were stopped because longer time might lead to the generation of cracks, which interferes with the next tests. It can be also seen that the corrosion rate determined by GC goes up rapidly after 50 days of test. This increase should be attributed to the development of cracks in the cement paste, which eventually led to the complete split of the cement paste into two parts (Figure 6(a)).

In condition 2, visible cracks can be observed in EC samples after 8 days (Figure 6(b)). These cracks propagated with time, leading to widely spread results in Figure 5(b). L.M. Spasova et al. [6] and Q. Zhou et al. [7] reported similar cracking phenomena regarding the corrosion of Al embedded BFS/OPC systems. This is attributed to the increasing internal stress generated by the production of H_2 gas and by the accumulation of the corrosion products involving volume changes compared to the pure Al phase. On the contrary, GC samples did not show any visible cracks, which could probably be attributed to the smaller size (15x15x1mm) of GC samples compared to the larger EIS samples (30x30x1mm). Besides, the steady corrosion rate in condition 2 is slightly higher than that in condition 1, which can be explained by the fact that the complete saturation of the cement

paste provided more water for the corrosion reaction in condition 2. The SEM characterization applied to pure OPC samples failed to provide trustworthy film thickness results. Firstly, the presence of holes and cracks led to the wide discrepancy of the film thickness results at different locations (see Section 3.5); secondly, it was difficult to identify the boundary between the cement paste and the corrosion product film in some samples. Therefore, no corrosion rate calculated from SEM data for pure OPC samples is reported in Figure 5.

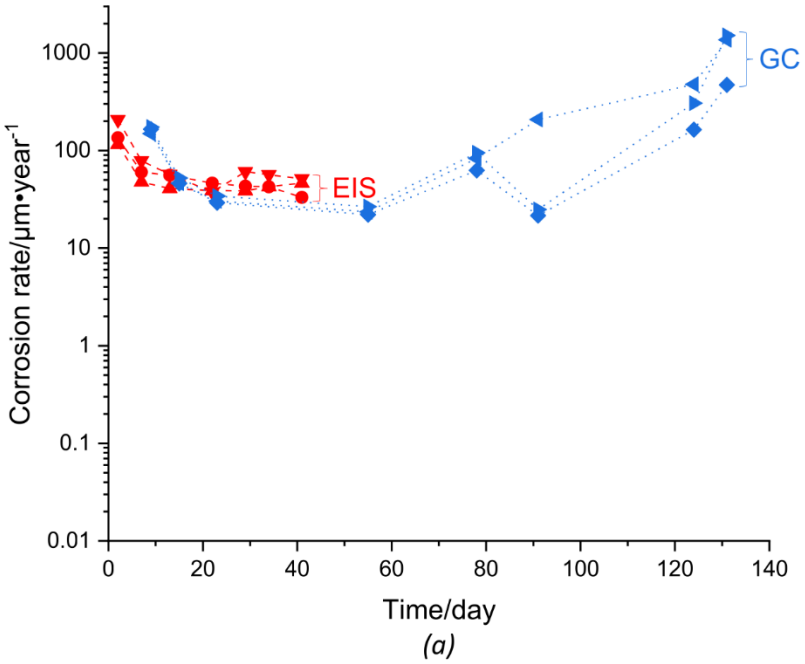

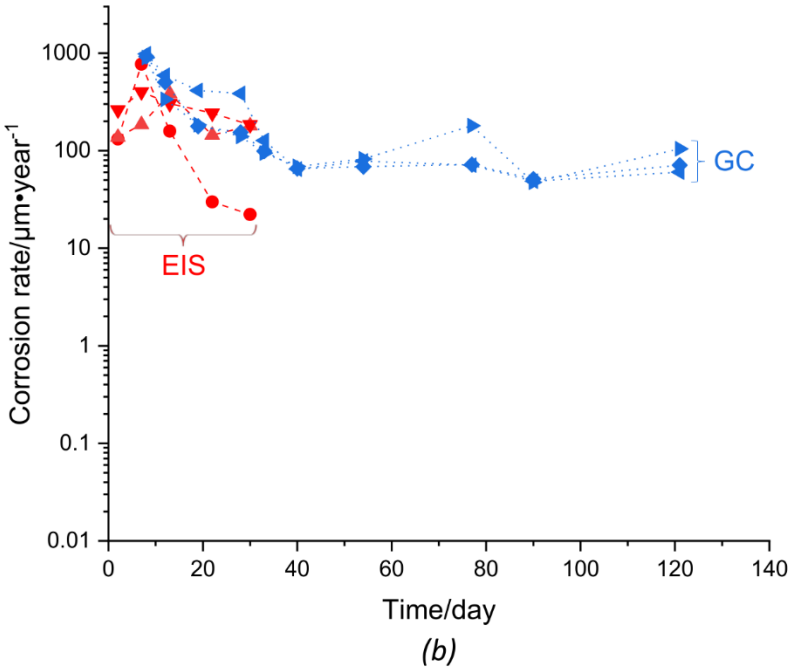

Figure 5. Variation of the corrosion rates as a function of time of (a) OPC samples in condition 1, (b) OPC samples in condition 2.

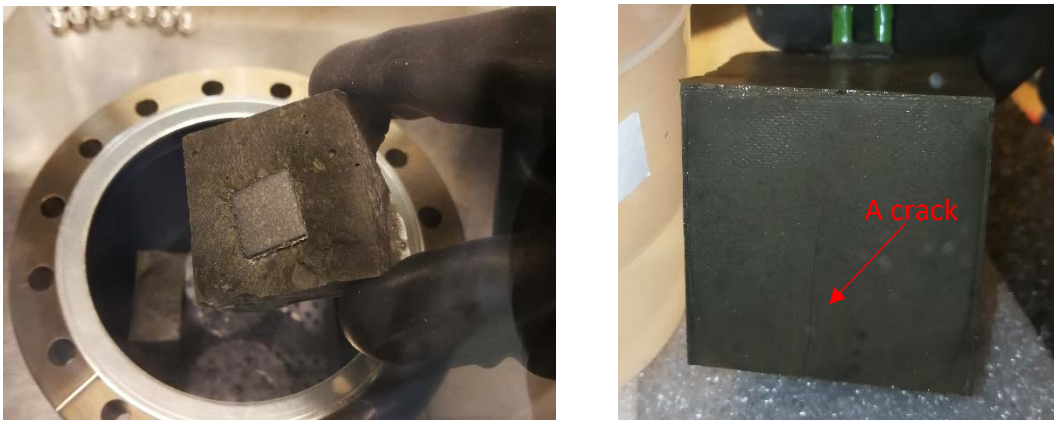

(a) (b)

Figure 6. Pictures showing (a) the breach of a GC sample in condition 1 after 133 days and (b) a crack in an EC sample appeared in condition 2 generated after 8 days.

On the basis of the results mentioned above and the mechanisms proposed in literature [41,42], the corrosion process of pure OPC samples can be hypothesized as shown in Figure 7. After the preceding oxide layer is consumed, the corrosion of aluminium initiates with the formation of aluminium hydroxide gel and hydrogen gas. Aluminium hydroxide immediately reacts with hydroxyl ion to form $Al(OH)_4^-$ in the highly alkaline pore solution of the cement paste [41]. Considering the microstructure of the cement paste, the generated $Al(OH)_4^-$ ions are difficult to be thoroughly dissolved in the pore solution (insufficient amount of pore solution at the interface) or completely diffuse into the cement paste matrix (the constrained diffusion path). Therefore, $Al(OH)_4^-$ ions are most likely to precipitate as hydroxoaluminate salts at the interface to form the corrosion product film. The possible ions (Ca^{2+}, Mg^{2+}, Zn^{2+}, etc.) in the cement paste could also lead to the formation of LDH films [43-45]. For example, literature reported that Al can react with $Ca(NO_3)_2$ solution in alkaline condition (pH 10) to form Ca-Al layered double hydrates ($[CaAl_2(OH)_6]_n^{2+} \cdot 2X^{n-} \cdot yH_2O$, where X^{n-} can be NO_3^- or other anions) [43]. Therefore, this corrosion product film could be a mixture of hydroxoaluminate salts and layered double hydrates, which does not show good corrosion-resistant ability. Meanwhile, the diffusion direction of Al ions is from the interface to the cement paste, which leads to the formation of Strätlingite in the cement paste [41]. The corrosion products such as H_2 gas raise the internal stress and consequently induce cracks in the cement paste matrix.

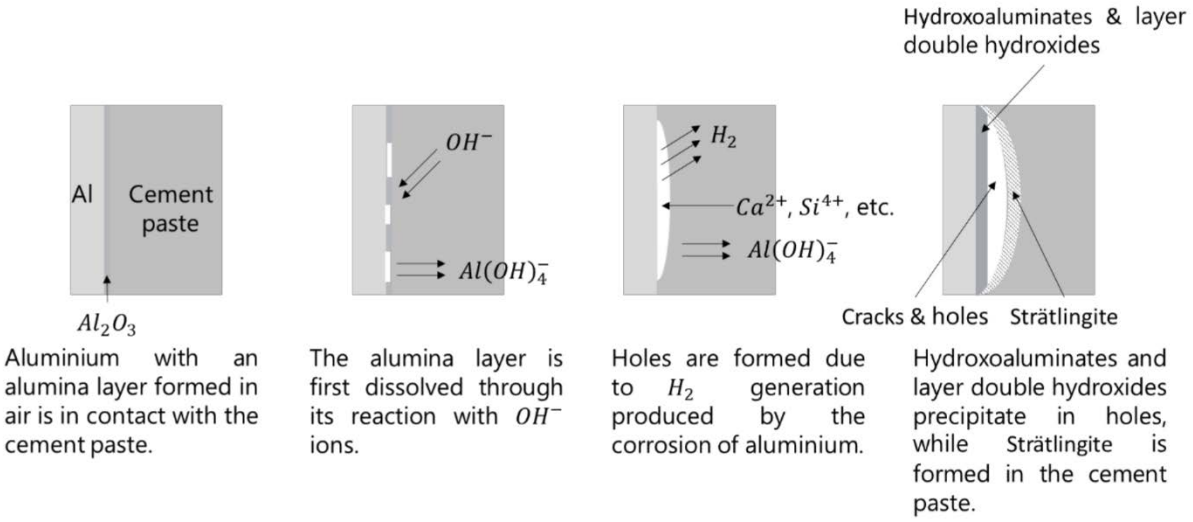

Figure 7. Anticipated scenario for the corrosion process of Al in the pure OPC paste.

Figure 8 provides the corrosion rates measured for OPC+$LiNO_3$ samples. The magnitude and variation of the corrosion rates with time from EIS and SEM techniques are comparable in both conditions. Initially, the corrosion rate decreases until reaching a steady state value around 10-20 µm y^{-1}. Note that in condition 1, a bump in the graph can be observed after 80 days when the samples were transferred from the humid argon atmosphere into the limewater. However, the corrosion rate decreases back fast to the steady state value observed before the transfer. This decrease could be due to the fast growth of the corrosion product film associated to a high corrosion rate. Later, the thicker film retards the corrosion rate. Compared to pure OPC samples, the OPC+$LiNO_3$ samples exhibited a lower corrosion rate while no visible cracks were observed, which indicates that the formation of the Li-Al LDH film improved the corrosion protection performance. [16]

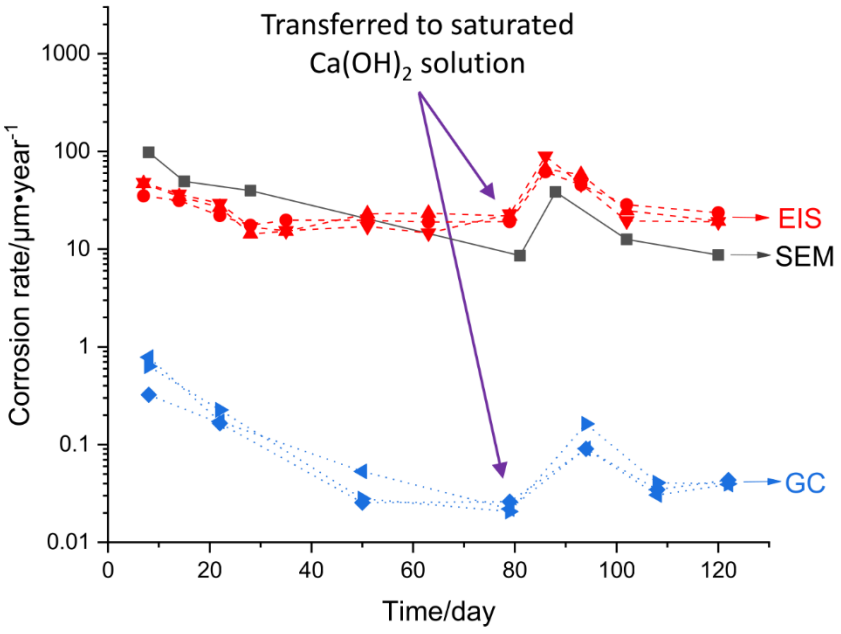

(a)

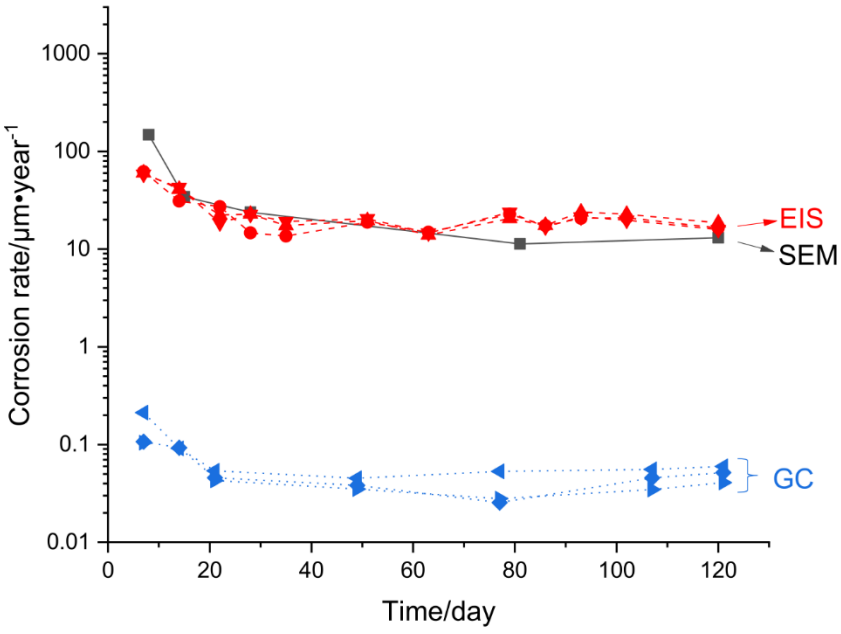

(b)

Figure 8. Variation of the corrosion rates as a function of time of (a) OPC+$LiNO_3$ samples in condition 1, (b) OPC+$LiNO_3$ samples in condition 2.

The results also show that although the corrosion rates measured with GC follow the same trend as those obtained from EIS and SEM (including the peak in the corrosion rate when the sample was transferred to saturated $Ca(OH)_2$), the values of the corrosion rate obtained from GC are about 2 orders of magnitude lower than those from EIS and SEM. This matches the findings of

Matsuo et al. [12,13] and Delpech et al. [14], which showed that the corrosion rate obtained from GC is several orders of magnitude smaller than the one obtained from impedance spectroscopy [14] and could be as low as a few micro meters per year [12]. A possible reason for the discrepancy between the corrosion rate values determined by EIS/SEM and GC could be the fact that in the presence of nitrate, the corrosion of aluminium mainly produces aluminates and ammonium, instead of hydrogen [46], as follow:

$$8Al + 3NO_3^- + 5OH^- + 18H_2O \rightarrow 8Al(OH)_4^- + 3NH_3\ . \qquad (6)$$

Because the calculation of the corrosion rate is merely based on the generation of H_2 (Eq. (3)), an underestimation of the gas production results in the abnormally low corrosion rate from GC.

For OPC+Li_2CO_3 samples in condition 1 (see Figure 9(a)), the corrosion rates gathered from the three different techniques are in good agreement until the immersion of the samples in limewater (after 80 days). The corrosion rate of the samples decreased from around 600 µm·y^{-1} to around 20 µm·y^{-1}. This decline is sharper at the beginning and slowed down afterwards. This trend could be attributed to two possible mechanisms: (1) the accumulation of the protective corrosion product film decreases the corrosion rate; (2) the lower water content and porosity of the cement paste, as a function of its hydration process, decreases the corrosion rate. After 80 days, when the samples were immersed in saturated $Ca(OH)_2$ solution, the corrosion rate determined by EIS and SEM increased rapidly until reaching a plateau at 70-100 µm·y^{-1}. However, when looking at the data obtained from GC measurements, triplicated GC samples begin to show significant discrepancies and the corrosion rates irregularly fluctuates in the range of 0.1 µm·y^{-1} to 20 µm·y^{-1}. For condition 2, both EIS and SEM show a sharp decrease of the corrosion rate in the first days before slightly rising back to reach values around 70-90 µm·y^{-1} after ~120 days. These corrosion rates are equivalent to the one observed in condition 1 after the immersion in $Ca(OH)_2$ solution. Note that the corrosion rate decreases more and for a longer period when it is extracted from SEM micrographs compared to EIS before to reach comparable values. A possible explanation for this difference can be the influence of the delamination of the corrosion product film, because a delamination phenomenon was found by SEM characterisation in parts of the corrosion product film after 30 days and became more severe with time. The different delamination states (when

and where the delamination occurred, how fast they developed, etc.) in distinctive samples can therefore lead to the different corrosion rates that have been measured in this study. More information about this delamination process is provided in Section 3.5. Regarding the triplicate GC samples, they provided different corrosion rates without a clear varying trend. It seems that the immersion of the samples in saturated $Ca(OH)_2$ solution induces a change in the corrosion mechanism resulting in perturbation in the hydrogen production and therefore, to the determination of the corrosion rate by GC in both curing conditions. It is still difficult to understand the detailed mechanisms behind the erratic GC results and further research is needed to better understand the phenomenon encountered.

Generally, OPC+Li_2CO_3 samples exhibit a higher corrosion rate compared to OPC+$LiNO_3$ samples. However, it is difficult to compare the effectiveness of Li_2CO_3 and $LiNO_3$ in cement pastes directly, because the higher water content associated to the larger water/cement ratio (0.5) in OPC+Li_2CO_3 samples can escalate the corrosion rate.

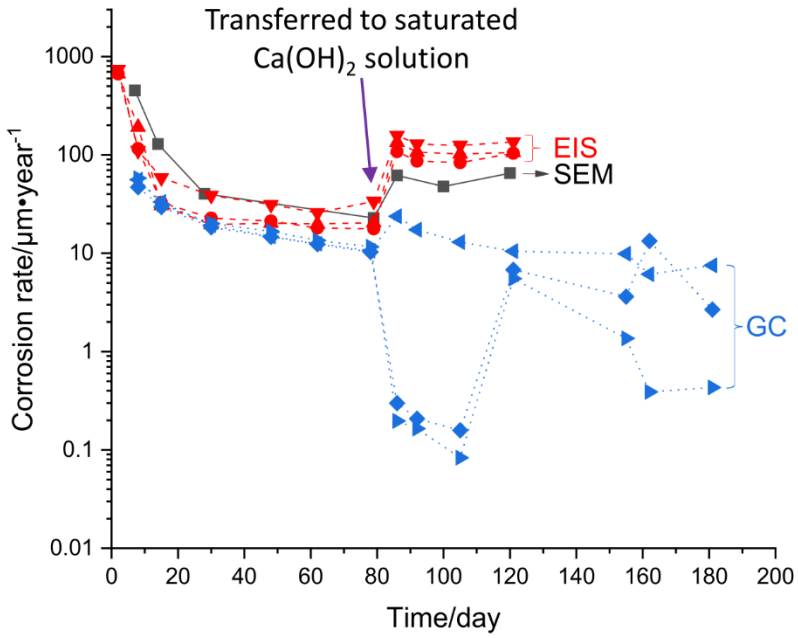

(a)

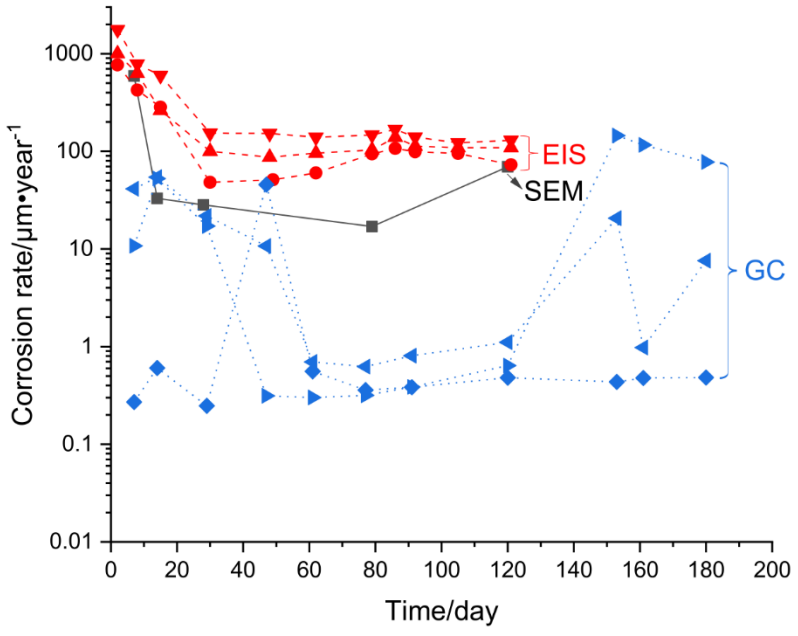

(b)

Figure 9. Variation of the corrosion rates as a function of time of (a) OPC+Li_2CO_3 samples in condition 1, (b) OPC+Li_2CO_3 samples in condition 2.

3.4. The resistance of the corrosion product film (R_f)

R_f is the resistance of the corrosion product film as determined from the impedance spectrum fitting. R_f is normally proportional to the film thickness, the thicker the film is, the higher the R_f value is. Besides, due to the porous structure of LDH films, the intrusion of outer solution could

significantly decrease the R_f value by filling the pores [43-45]. Therefore, although R_f is not the only decisive factor, it reveals the protection ability of the corrosion product film to some extent and studying its variation with time could give important information in relation with the corrosion mechanism of AA1100 in contact with cement pastes.

The R_f results of pure OPC samples gathered from EIS fitting are shown in Figure 10. For samples in condition 1 (Figure 10(a)), the R_f values gradually increase until 13 days to reach a value around 5000 ohm·cm^2, which could be attributed to the increase of the thickness of the film. Afterwards, R_f drops to about 1000 ohm·cm^2 and remains constant. A possible explanation is that the corrosion products contain more and more solution. This increasing water content can be caused by many factors e.g. the amount of water used for corrosion reactions is reduced because of the decrease of the corrosion rate, or the high humid outer atmosphere provides extra water into the sample by condensation. As explained earlier, the R_f values of the film in condition 2 are significantly influenced by the rapid propagation of cracks in the cement paste, leading to non-repetitive results, as shown in Figure 10(b).

Figure 10(c) and (d) show the variation of R_f values of the OPC+$LiNO_3$ samples. For condition 1 (Figure 10(c)), R_f decreases from a high level (~40000 ohm·cm^2) at the beginning to about 2000 ohm·cm^2 until the cement paste sample was immersed in saturated $Ca(OH)_2$ after 80 days. After the immersion of the sample in saturated $Ca(OH)_2$, an apparent drop of R_f occurs within 14 days after the immersion, which could be attributed to the fact that the LDH film got gradually saturated with $Ca(OH)_2$ solution, decreasing its resistance. After this drop, R_f increases again because of the accelerated corrosion of the Al causing a thickening of the corrosion product film, which inevitably leads to an increase of the resistance of the corrosion product film. In condition 2, R_f drops down significantly during the first days of the tests, which is assumed to be caused by the increasing amount of solution in the film, to reach a fairly constant value afterwards. It was also observed that the steady-state value of R_f, measured at the end of the testing period, was similar for both conditions, i.e. around 1000 ohm·cm^2.

The R_f results, obtained for OPC+Li_2CO_3 are shown in Figure 10(e) and (f). In condition 1, R_f rapidly decreases from 3000 ohm·cm^2 to about 100 ohm·cm^2. This sharp decrease is likely due to the

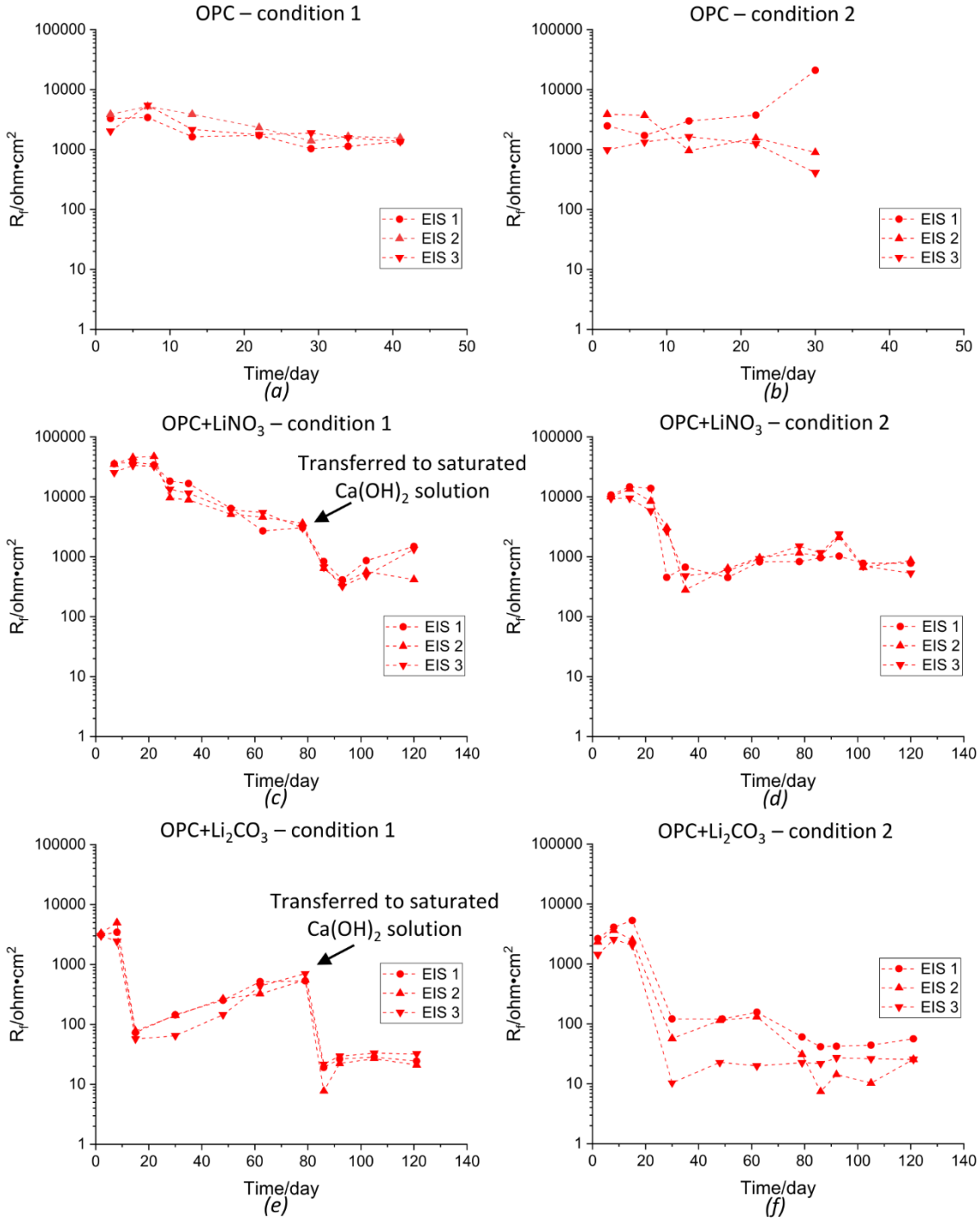

Figure 10. Evolution of R_f as a function of time of (a) OPC samples in condition 1, (b) OPC samples in condition 2, (c) OPC+$LiNO_3$ samples in condition 1, (d) OPC+$LiNO_3$ samples in condition 2, (e) OPC+Li_2CO_3 samples in condition 1, (f) OPC+Li_2CO_3 samples in condition 2.

ingress of solution into the film. Afterwards, the growth of the film raises R_f until the immersion of the sample in $Ca(OH)_2$ solution after 80 days, which leads to a significant decrease of R_f. Then, R_f remains constant after this drop. This final steady state is in contradiction with SEM

characterisation, which shows a continuous increase of the film thickness. Meanwhile, the delamination occurs after the immersion. Therefore, it is assumed that this R_f drop after the immersion is dominated by delamination. In condition 2, a rapid R_f decrease occurs between the 20th day and the 28th day, which is attributed to the delamination observed by SEM after 28 days. Then R_f remains constant with a slight decrease at the end of the test. R_f values in both conditions end at a low level (around 30-40 ohm·cm^2), which is significantly lower than that in other cement pastes. This could also be explained by the delamination: after delamination, only the resistance of the thin newly born film on the Al surface counted as R_f in the EIS fitting.

The analytics of R_f results are supported by literature. The R_f values presented in Figure 10 decrease sharply after the initial period or after the immersion in $Ca(OH)_2$ solution. The same decrease is found in the impedance study of different Al based LDH films immersed in solutions [43-45]. This decrease is believed to be caused by the ingress of the electrolyte, replacing the trapped air in the porous structure of the LDH film. This intrusion process of the eletrolyte decreases the film resistance. Iqbal et al. reported that an impedance decrease by at least one order of magnitude occurred within 7 days after the immersion in NaCl solution in the impedance study of CaAl-LDH films [43] and MgAl-LDH [44]. Cao et al. [45] found that the impedance of ZnAl-LDH films kept stable up to 21 days in NaCl solution and decreased dramatically after 28 days.

3.5. Observation of the Al/corrosion product film/cement paste interface by Scanning Electron Microscopy (SEM)

SEM characterisation was performed to determine the thickness of the corrosion product film, which is used to calculate the corrosion rate as introduced in Section 2.2.

Table 2 provides the film thickness values as a function of time for OPC+$LiNO_3$ and OPC+Li_2CO_3 samples (the thickness determination of pure OPC samples was interfered by cracks and holes). The film thickness monotonically increases in all cases, even after the immersion of $Ca(OH)_2$ solution in condition 1. This means that the immersion of $Ca(OH)_2$ solution cannot dissolve the film. On the contrary, the thickness of the corrosion product film has an obvious instantaneous

increase after the immersion, which is attributed to the increase of corrosion rate when more solution is available for the corrosion rate.

Table 2. The variation of the film thickness as a function of time for OPC+$LiNO_3$ and OPC+Li_2CO_3 samples from SEM characterisation.

OPC+$LiNO_3$		Condition 1 (transferred to $Ca(OH)_2$ solution on the 81th day)							Condition 2					
	Time/day	8	15	28	81	88	102	120	8	15	28	81	120	
	Film thickness/µm	2.1	3.1	4.5	5.7	6.5	7.0	7.4	3.3	3.9	4.8	6.4	7.8	
OPC+Li_2CO_3		Condition 1 (transferred to $Ca(OH)_2$ solution on the 79th day)							Condition 2					
	Time/day	7	14	28	79	86	100	120	8	14	28	79	120	
	Film thickness/µm	8.7	11.2	12.7	15.9	17.1	18.9	22.5	13.0	13.5	14.6	17.0	24.8	

The morphology of the cement paste/corrosion product film/Al interface has also been studied by scanning electron microscopy. SEM images of three types of samples after 28 days in condition 2 are shown in Figure 11. (The results in condition 1 are provided in Figure S7 in Part 6 of the supplementary material)

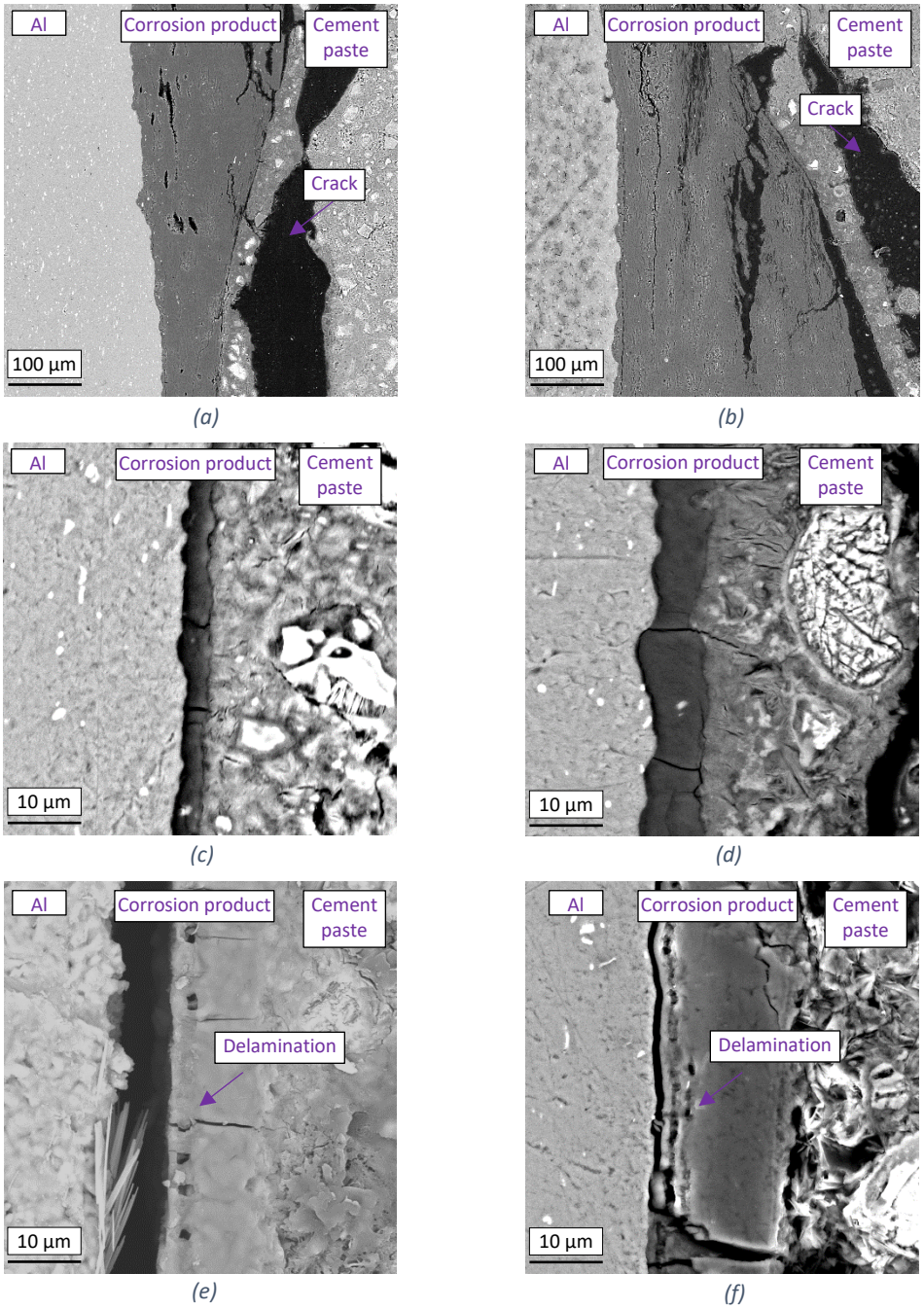

Figure 11. SEM micrographs of (a) the pure OPC sample after 28 days, (b) the pure OPC sample after 79 days, (c) the OPC+$LiNO_3$ sample after 28 days, (d) the OPC+$LiNO_3$ sample after 79 days, (e) the OPC+Li_2CO_3 sample after 28 days, (f) the OPC+Li_2CO_3 sample after 79 days, in condition 2.

In terms of pure OPC samples, it can be clearly seen in Figure 11(a) and (b) that cracks and holes formed in the cement paste near the interface. Meanwhile, the thickness of the corrosion product film varied significantly, leading to the difficulties in the determination of the average thickness value.

Figure 11(c) and (d) provide SEM micrographs of OPC+$LiNO_3$ samples. In these samples, the corrosion product film is thin and dense.

As introduced before, delamination has been observed in some OPC+Li_2CO_3 samples. In condition 1, delamination is found only after the immersion in $Ca(OH)_2$ solution. In condition 2, delamination is firstly observed after 28 days and it further proceeds as a function of time (see Figure 11(e) and (f)). In OPC+Li_2CO_3 samples, the main component of the corrosion product film is assumed to be Li-Al layered double hydroxide. According to SEM characterization, it seems that the Li-Al LDH film is prone to delaminate and form a newly born film when the thickness of the old film reaches a certain value.

To try to further understand the mechanism, a line-scan analysis was performed by EDX to gain information on the evolution of the elemental concentration inside the corrosion product layer. Figure 12 shows the content distributions of 4 kinds of elements (Al, O, Ca and Si) of the cross-section of the OPC+Li_2CO_3 sample after 79d in condition 2. The distributions of Al and O indicate the boundaries of the different phases (Al/corrosion product film/cement paste), while Ca and Si are typical elements in the cement paste, which tend to diffuse from the cement paste towards the corrosion product film. The Al content significantly decreases on the aluminium/corrosion product film boundary, while the O content dramatically rises. The sharp changes of Al and O are localized in the small district near the boundary, the other part of the corrosion product film has almost fixed contents of Al (about 30%) and O (about 60%). This Al:O ratio (1:2) is higher than the ones of standard LDH films (hydrates lead to a high oxygen content). This can be explained by two possible mechanisms. Firstly, the corrosion product film is a complex mixture with other constitutes such as Al_2O_3 and hydroxoaluminates decreasing the overall Al:O ratio. Secondly, EDX is a semi-quantitative technique, leading to some uncertainty on the elemental concentration. Ca and Si diffuse from the cement paste (the high concentration region) to the corrosion product film (the low concentration region). Moreover, the Ca concentration sharply decreases at the interface between the cement paste and the corrosion product film. Afterwards, the Ca concentration is gradually decreasing until reaching the surface of AA1100. The evolution of the Si concentration is similar to the one of Ca. Its content declines from the cement paste to the corrosion product film. However, contrary to the Ca concentration, the Si concentration reaches

zero near the delamination surface (the boundary between the old film and the newly born film) and not on the surface of AA1100. This could be explained by the fact that Si diffusion is hindered by delamination. Additional EDX results (in Part 6 of the supplementary material) provide more evidences that Si diffusion follows different rules on the two sides of the delamination inside the corrosion product film. One possible explanation is that the delamination creates a new interface and hence interferes the Si diffusion.

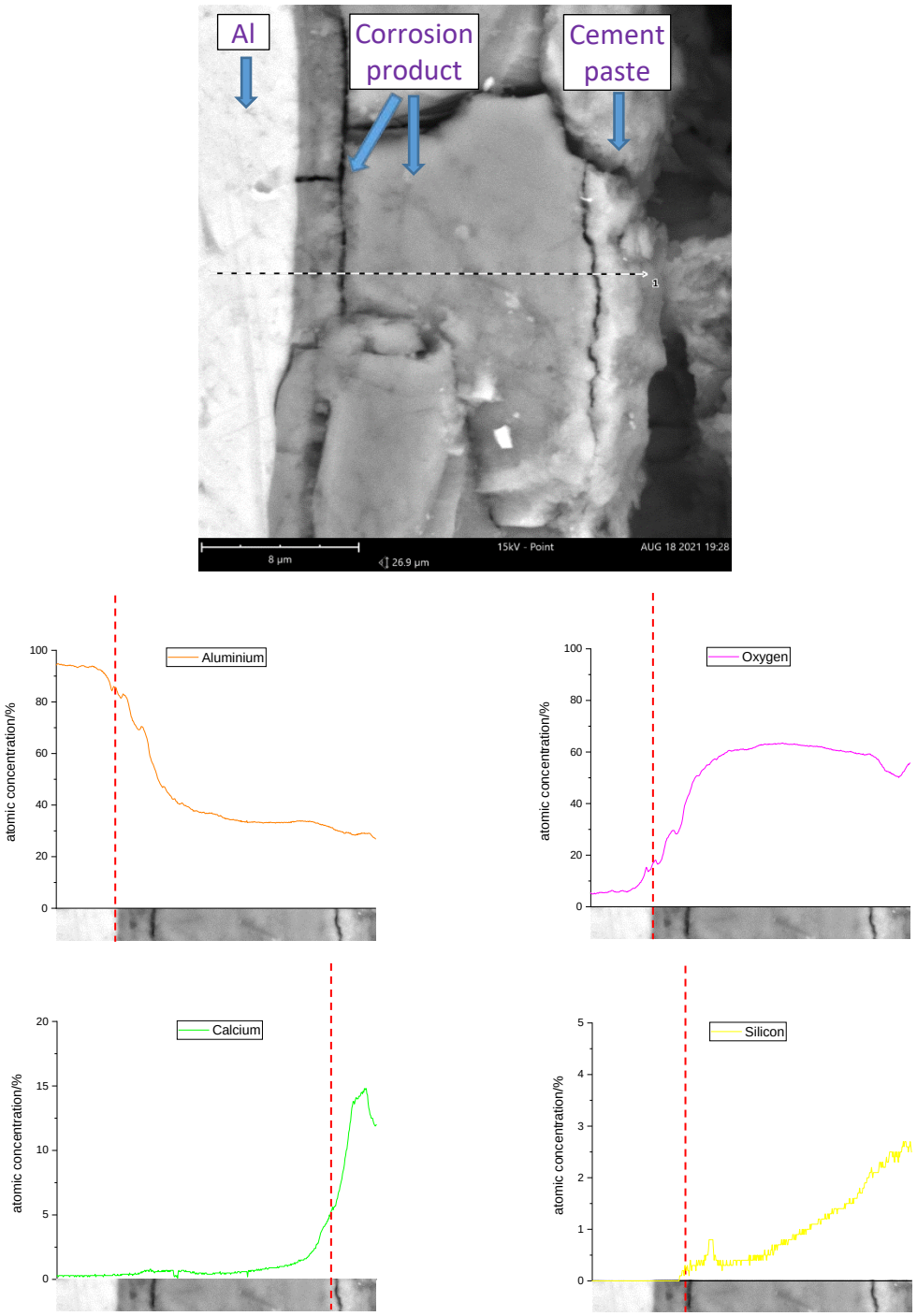

Figure 12. EDX line scan results (Al, O, Ca and Si) of the cross-section of a OPC+Li_2CO_3 sample after exposure to saturated $Ca(OH)_2$ (condition 2) for 79 days.

4. Conclusion

The corrosion inhibition effect of $LiNO_3$ and Li_2CO_3 on AA1100 in OPC pastes has been studied by a combination of different methods. The main findings of the study are the following:

1. In general, the corrosion rates determined by different techniques i.e. EIS, SEM and GC, support each other, enhancing the reliability of the data.
2. The use of hydrogen production determined by GC for studying the corrosion rate possibly provides misleading results. For example, in presence of $LiNO_3$, the corrosion mechanism differs and NH_3 is produced instead of H_2, leading to underestimated corrosion rates of samples with $LiNO_3$ addition.
3. Both $LiNO_3$ and Li_2CO_3 are effective corrosion inhibitors for Al in cement pastes. Indeed, no cracks are generated in the cement paste matrix when adding $LiNO_3$ or Li_2CO_3. However, $LiNO_3$ is more suitable for the encapsulation of Al in the cement paste, because the combination of 0.36 water/cement ratio and 3 wt.% $LiNO_3$ provides the lowest corrosion rates without any curing problems. The low and predictable level of hydrogen production of OPC+$LiNO_3$ samples is also beneficial to the long-term encapsulation.
4. The ingress of saturated $Ca(OH)_2$ solution significantly increases the corrosion rate of Al in cement pastes.
5. The variation of the resistance of the corrosion product film is associated to the thickness and the water content of the film. With the ingress of the electrolyte into the film, the resistance decreases gradually.
6. Delamination is observed in samples with Li_2CO_3 addition when the thickness of the corrosion product film reaches a critical value. This phenomenon significantly impacts on the corrosion rate and seems to be related to elements' diffusion. Detailed mechanisms need further researches.

References

1. A. Leenaers, C. Detavernier and S. Van den Berghe, The effect of silicon on the interaction between metallic uranium and aluminum: A 50 year long diffusion experiment. Journal of nuclear materials, 381 (3) (2008) 242-248.
2. C. Azevedo, Selection of fuel cladding material for nuclear fission reactors, Engineering Failure Analysis, 18 (2011) 1943-1962.
3. B. Kursten, F. Druyts, D. Macdonald, N. Smart, R. Gens, L. Wang, E. Weetjens, J. Govaerts, Review of corrosion studies of metallic barrier in geological disposal conditions with respect to Belgian Supercontainer concept, Corrosion Engineering, Science and Technology, 46 (2011) 91-97.
4. M. Ochs, D. Mallants, L. Wang, Radionuclide and metal sorption on cement and concrete, Springer, 2016.
5. M. Pourbaix, Atlas of electrochemical equilibria in aqueous solution, NACE, 307 (1974).
6. L. Spasova, M. Ojovan, Characterisation of Al corrosion and its impact on the mechanical performance of composite cement wasteforms by the acoustic emission technique, Journal of Nuclear Materials, 375 (2008) 347-358.
7. Q. Zhou, N.B. Milestone, M. Hayes, An alternative to Portland Cement for waste encapsulation--the calcium sulfoaluminate cement system, J Hazard Mater, 136 (2006) 120-129.
8. E. Michailidou, P. Visser, J.M.C. Mol, A. Kosari, H. Terryn, K. Baert, Y. Gonzalez-Garcia, The Effect of pH on the Corrosion Protection of Aluminum Alloys in Lithium-carbonate-containing NaCl Solutions, Corrosion Science, (2022) 110851.
9. J. Gui, T. Devine, Influence of lithium on the corrosion of aluminum, Scr. Metall.;(United States), 21 (1987).
10. R.G. Buchheit, M. Bode, G. Stoner, Corrosion-resistant, chromate-free talc coatings for aluminum, Corrosion, 50 (1994) 205-214.

11. C. Drewien, M. Eatough, D. Tallant, C. Hills, R. Buchheit, Lithium-aluminum-carbonate-hydroxide hydrate coatings on aluminum alloys: Composition, structure, and processing bath chemistry, Journal of materials research, 11 (1996) 1507-1513.

12. T. Matsuo, T. Izumida, M. Hironaga, Y. Horikawa, T. Shiomi, $LiNO_3$ Effect on Corrosion Prevention of Aluminum with Complex Shapes, Journal of Nuclear Science and Technology, 34 (1997) 823-828.

13. T. Matsuo, T. Nishi, M. Matsuda, T. Izumida, $LiNO_3$ addition to prevent hydrogen gas generation from cement-solidified aluminum wastes, Journal of nuclear science and technology, 32 (1995) 912-920.

14. S. Delpech, C. Cannes, N. Barré, Q.T. Tran, C. Sanchez, H. Lahalle, D. Lambertin, S. Gauffinet, C.C.D. Coumes, Kinetic Model of Aluminum Behavior in Cement-Based Matrices Analyzed by Impedance Spectroscopy, Journal of The Electrochemical Society, 164 (2017) 717-727.

15. G.R. Williams, D. O'Hare, A kinetic study of the intercalation of lithium salts into $Al(OH)_3$, The Journal of Physical Chemistry B, 110 (2006) 10619-10629.

16. M.A. Iqbal, L. Sun, A.T. Barrett, M. Fedel, Layered Double Hydroxide protective films developed on aluminum and aluminum alloys: Synthetic methods and anti-corrosion mechanisms, Coatings, 10 (2020) 428.

17. T. Matsuo, K. Kobayashi, K. Tago, Estimation of the solubility dependence of aluminate salts of alkali metals on ion radii of alkali metals by LDF molecular orbital calculations, The Journal of Physical Chemistry, 100 (1996) 6531-6542.

18. T. Matsuo, M. Matsuda, M. Hironaga, Y. Horikawa, Effect of $LiNO_3$ on corrosion prevention of aluminum wastes after their land disposal, Journal of nuclear science and technology, 33 (1996) 852-862.

19. T. Matsuo, T. Izumida, M. Hironaga, Y. Horikawa, T. Shiomi, Aluminum corrosion under alkaline circumstances while $LiNO_3$ concentration is lowered, Journal of nuclear science and technology, 35 (1998) 226-233.

20. Y. Liu, P. Visser, X. Zhou, S.B. Lyon, T. Hashimoto, M. Curioni, A. Gholinia, G.E. Thompson, G. Smyth, S.R. Gibbon, Protective film formation on AA2024-T3 aluminum

alloy by leaching of lithium carbonate from an organic coating, Journal of The Electrochemical Society, 163 (2015) 45.

21. C. Rangel, M. Travassos, The passivation of aluminium in lithium carbonate/bicarbonate solutions, Corrosion science, 33 (1992) 327-343.
22. P. Visser, H. Terryn, J.M. Mol, On the importance of irreversibility of corrosion inhibitors for active coating protection of AA2024-T3, Corrosion Science, 140 (2018) 272-285..
23. P. Visser, Y. Gonzalez-Garcia, J.M. Mol, H. Terryn, Mechanism of passive layer formation on AA2024-T3 from alkaline lithium carbonate solutions in the presence of sodium chloride, Journal of The Electrochemical Society, 165 (2018) 60.
24. P. Visser, Y. Liu, X. Zhou, T. Hashimoto, G.E. Thompson, S.B. Lyon, L.G. van der Ven, A.J. Mol, H.A. Terryn, The corrosion protection of AA2024-T3 aluminium alloy by leaching of lithium-containing salts from organic coatings, Faraday Discussions, 180 (2015) 511-526.
25. J. Zapała-Sławeta, Z. Owsiak, The role of lithium compounds in mitigating alkali-gravel aggregate reaction, Construction and Building Materials, 115 (2016) 299-303.
26. S. Diamond, Unique response of $LiNO_3$ as an alkali silica reaction-preventive admixture, Cement and Concrete Research, 29 (1999) 1271-1275.
27. İ. Demir, Ö. Sevim, İ. Kalkan, Microstructural properties of lithium-added cement mortars subjected to alkali–silica reactions, Sādhanā, 43 (2018).
28. M. Wu, X. Lin, T. Wang, J. Qiu, T. Ma, Low-cost dye-sensitized solar cell based on nine kinds of carbon counter electrodes, Energy & Environmental Science, 4 (2011) 2308-2315.
29. X. Zhu, L.F. Macía, J. Jaguemont, J. de Hoog, A. Nikolian, N. Omar, A. Hubin, Electrochemical impedance study of commercial $LiNi_{0.80}Co_{0.15}Al_{0.05}O_2$ electrodes as a function of state of charge and aging, Electrochimica acta, 287 (2018) 10-20.
30. S. Caes, A.C. Gurning, X. Li, V. de Souza, B. Kursten, Corrosion of aluminium in ordinary Portland cement paste: Influence of matrix porosity and the presence of $LiNO_3$ corrosion inhibitor, Materials and Corrosion, (2022).

31. M. Stern, A.L. Geary, Electrochemical polarization: I. A theoretical analysis of the shape of polarization curves, Journal of the electrochemical society, 104 (1957) 56.

32. T.A. Zawodzinski, JES Classics, Electrochemical Society Interface, (2009) 59.

33. L. Woo, S. Wansom, A. Hixson, M. Campo, T. Mason, A universal equivalent circuit model for the impedance response of composites, Journal of materials science, 38 (2003) 2265-2270.

34. B. Díaz, B. Guitián, X.R. Nóvoa, C. Pérez, Conductivity assessment of multifunctional cement pastes by impedance spectroscopy, Corrosion Science, 185 (2021) 109441.B. Díaz, L. Freire, P. Merino, X. Nóvoa, M. Pérez, Impedance spectroscopy study of saturated mortar samples, Electrochimica acta, 53 (2008) 7549-7555.

35. B. Díaz, L. Freire, P. Merino, X. Nóvoa, M. Pérez, Impedance spectroscopy study of saturated mortar samples, Electrochimica acta, 53 (2008) 7549-7555.

36. G. Song, Equivalent circuit model for AC electrochemical impedance spectroscopy of concrete, Cement and concrete research, 30 (2000) 1723-1730.

37. A. Xu, Y. Weng, R. Zhao, Permeability and equivalent circuit model of ionically conductive mortar using electrochemical workstation, Materials, 13 (2020) 1179.

38. B. Dong, Q. Qiu, J. Xiang, C. Huang, F. Xing, N. Han, Study on the carbonation behavior of cement mortar by electrochemical impedance spectroscopy, Materials, 7 (2014) 218-231.

39. M. Shi, Z. Chen, J. Sun, Determination of chloride diffusivity in concrete by AC impedance spectroscopy, Cement and Concrete Research, 29 (1999) 1111-1115.

40. R. Vedalakshmi, V. Saraswathy, H.-W. Song, N. Palaniswamy, Determination of diffusion coefficient of chloride in concrete using Warburg diffusion coefficient, Corrosion Science, 51 (2009) 1299-1307.

41. A. Setiadi, N.B. Milestone, J. Hill, M. Hayes, Corrosion of aluminium and magnesium in BFS composite cements, Advances in Applied Ceramics, 105 (2013) 191-196.

42. H. Godfrey, M. Hayes, D. Anderson, S. Rawlinson, J. Borwick, J. Clifford, Corrosion of 1050, 1085, and 5083 grade aluminium in the pore water of a GGBS/CEM I grout up to 777 d, Journal of Nuclear Materials, 515 (2019) 257-266.

43. M.A. Iqbal, L. Sun, A.M. LaChance, H. Ding, M. Fedel, In situ growth of a CaAl-NO_3^--layered double hydroxide film directly on an aluminum alloy for corrosion resistance, Dalton Transactions, 49 (2020) 3956-3964.
44. M.A. Iqbal, M. Fedel, Effect of synthesis conditions on the controlled growth of MgAl–LDH corrosion resistance film: structure and corrosion resistance properties, Coatings, 9 (2019) 30.
45. Y. Cao, D. Zheng, X. Li, J. Lin, C. Wang, S. Dong, C. Lin, Enhanced corrosion resistance of superhydrophobic layered double hydroxide films with long-term stability on Al substrate, ACS applied materials & interfaces, 10 (2018) 15150-15162.
46. J.C. Fanning, The chemical reduction of nitrate in aqueous solution, Coordination Chemistry Reviews, 199 (2000) 159-179.